

Calibrated acoustic emission system records M -3.5 to M -8 events generated on a saw-cut granite sample

McLaskey, G.C.

Cornell University, Ithaca, NY, USA

Lockner, D.A.

U.S. Geological Survey, Menlo Park, CA, USA

Copyright 2015 ARMA, American Rock Mechanics Association

This paper was prepared for presentation at the 49th US Rock Mechanics / Geomechanics Symposium held in San Francisco, CA, USA, 28 June-1 July 2015.

This paper was selected for presentation at the symposium by an ARMA Technical Program Committee based on a technical and critical review of the paper by a minimum of two technical reviewers. The material, as presented, does not necessarily reflect any position of ARMA, its officers, or members. Electronic reproduction, distribution, or storage of any part of this paper for commercial purposes without the written consent of ARMA is prohibited. Permission to reproduce in print is restricted to an abstract of not more than 200 words; illustrations may not be copied. The abstract must contain conspicuous acknowledgement of where and by whom the paper was presented.

ABSTRACT: Acoustic emission (AE) analyses have been used for decades for rock mechanics testing, but because AE systems are not typically calibrated, the absolute sizes of dynamic microcrack growth and other physical processes responsible for the generation of AEs are poorly constrained. We describe a calibration technique for the AE recording system as a whole (transducers + amplifiers + digitizers + sample + loading frame) that uses the impact of a 4.76 mm free-falling steel ball bearing as a reference source. We demonstrate the technique on a 76 mm diameter cylinder of westerly granite loaded in a triaxial deformation apparatus at 40 MPa confining pressure. In this case, the ball bearing is dropped inside a cavity within the sample while inside the pressure vessel. We compare this reference source to conventional AEs generated during shear loading of a saw-cut simulated fault in a second granite sample at confining pressures up to 120 MPa. All located AEs occur on the saw-cut surface and have moment magnitudes ranging from M -5.7 down to at least M -8. Dynamic events that rupture the entire simulated fault surface (stick-slip events) have measurable stress drop and macroscopic slip, and radiate seismic waves similar to those from a M -3.5 earthquake. The largest AE events that do not rupture the entire fault are M -5.7. For these events, we also estimate the corner frequency (200-300 kHz), and we assume the Brune earthquake source model to estimate source dimensions of 4-6 mm. These AE sources are larger than the 0.2 mm grain size and smaller than the 76 x 152 mm fault surface. Finally, we compare our results to other calibrated AE studies performed on different loading machines and discuss reasons for the observed maximum AE magnitude.

1. INTRODUCTION

Acoustic emissions (AEs) are tiny seismic events thought to be caused by microcracking or slip instability on the grain scale. They are sometimes recorded during rock mechanics experiments to monitor fracture and faulting processes [1]. In slow loading experiments on rock samples containing pre-existing artificial faults, AEs tend to cluster around stick-slip instabilities (dynamic events that involve slip of the entire fault surface) in a manner reminiscent of foreshocks and aftershocks. It has long been assumed that AEs are in some sense small-scale versions of earthquakes and that they can provide insights into earthquake mechanics [2-5]. Yet, while earthquakes are routinely quantified by their seismic moment, only rarely is the absolute size of an AE determined. This is because AE recording systems are not typically calibrated.

There are a number of factors that lead to difficulty in calibrating an AE recording system. First, AE sensors are typically designed for sensitivity and simplicity. As a

result, their output is related to a complicated and frequency-dependent mixture of surface acceleration, velocity, and displacement. The same sensor may act as an accelerometer in one frequency band and a displacement sensor in another. Second, wave propagation is extremely complicated and difficult to model due to attenuation, scattering and mode conversions and reflections from sample boundaries. Additional complications include variable sensor coupling, nonlinear sensor response such as aperture effects, and the limited bandwidth of most AE preamplifiers that essentially induces a filtering effect on recorded signals. All of these factors must be accounted for in order to obtain an absolute measure of an AE source.

This lack of AE system calibration leads to a lack of transparency in acoustic emission analyses, and has inhibited the success of the technique as a whole. For example, without absolute measurements, it is extremely difficult for two researchers who use different sensors and/or recording systems to compare their results. The

lack of absolute measurements also makes it difficult to quantitatively link AEs to the physical mechanisms that generate them.

This paper describes recent techniques used to calibrate acoustic emission (AE) systems for rock mechanics testing. The absolute sizes and seismic moments of small AEs and stick-slip instabilities are then compared to other AEs recorded in calibrated laboratory experiments and to larger natural and mining induced earthquakes.

1.1 Waveform modeling approach

One way to analyze an AE system is to break it down into its components and account for each one individually until the only unknown that remains is the source ($m_{ij}(t)$) [6]. In this approach, which we term the AE waveform modeling approach, it is assumed that the complicated processes of wave propagation and transduction can be represented as a sequence of linear operators or linear systems as depicted in Figure 1a [7]. The solution to some of these linear systems can be determined theoretically; others must be determined empirically by introducing a known input and measuring the output.

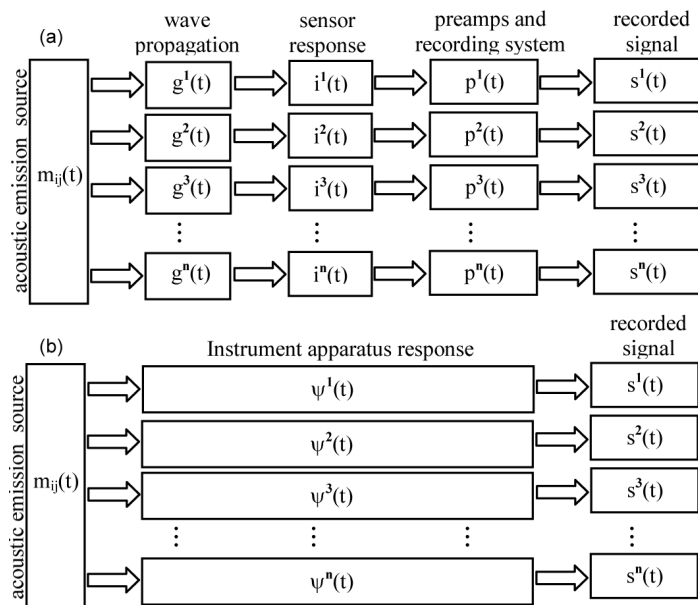


Fig. 1. Schematic diagram representing AE wave propagation and transduction. This process can either be (a) broken down into components that are systematically modeled or (b) lumped into a single system that is solved empirically with a well-defined reference source as an input.

For example, the box labeled "wave propagation" describes how an AE source causes a mechanical disturbance (i.e. surface displacements, velocities, accelerations) at the surface of the sample where the AE sensor is located. The solution to this linear system can be approximated by an elastodynamic Green's function, which can be calculated theoretically for some

geometries. Such a Green's function accounts for the linear elastic components of the wave propagation including geometrical spreading. Additional complications to wave propagation such as attenuation and scattering must be accounted for separately.

As a second example, the box labeled "sensor response" describes how a mechanical disturbance (surface displacements, velocities, etc.) is converted into a voltage signal. McLaskey and Glaser [8] demonstrated how to use this approach to calibrate AE sensors, and McLaskey et al. [9] used this technique to quantify AEs generated in a 2-m-sized granite sample where wave propagation was relatively easy to model. Yet, in general, it is very challenging to account for all of these components. Even the most rigorously calibrated AE systems grossly approximate, or omit entirely from the analysis, many of the complicated aspects of wave propagation and transduction such as attenuation, scattering, aperture effect, and sensor coupling [8].

1.2 Empirical calibration approach

An alternative approach, that we term the empirical AE system calibration approach, lumps all of these components (wave propagation, sensor response, preamps, etc.) together, treating them as a single linear system as shown in Figure 1b. This linear system is characterized solely by an input-output pair: a measured AE signal recorded in response to a reference seismic source with known characteristics. In some cases, a small AE can be used as a reference source for the analysis of a larger AE with a similar source location. This technique is essentially the same as the empirical Green's Function technique used for analyzing earthquakes [10-13]. Though this approach is quite powerful for estimating the corner frequency of AEs, it cannot be used for determining the absolute amplitude or seismic moment of the AE.

We go a step further and average together the output from each of the sensors. This averaging is performed in the frequency domain. It causes both the phase information and the directionality (focal mechanism) of the AE source to be lost, but it provides a more robust estimate of the amplitude of the AE source spectrum, which is then used to estimate the corner frequency and seismic moment of the AE. This averaging is also key to using a ball impact as an empirical calibration source. As opposed to a small AE, ball impact is an ideal reference source since both the absolute amplitude and shape of the source spectrum of the ball impact can be determined theoretically based on the geometry and kinematics of the collision [14, 8]. The directionality (or focal mechanism) of the ball impact is different from that of the AEs, but the modulating effects of directionality can

be reduced by the averaging, so that these differences do not significantly bias the calibration. Here it is assumed that the sensors adequately sample the focal sphere. Additionally, the averaging decreases sensitivity of the solution to differences in source location between the AE under analysis and the reference source. This is a convenient property of the technique, since ball impact sources can typically only be generated on the outer surface of a sample while AEs typically arise from within the interior of the sample. When appropriately applied, absolute amplitude of AEs can be estimated with this method to ± 0.2 magnitude units [15].

2. EXPERIMENT

We demonstrate the empirical calibration approach on a set of AE tests performed on a triaxial loading apparatus with principle stresses $\sigma_1 > \sigma_2 = \sigma_3$. The test sample was a cylinder of Westerly granite 76.2 mm in diameter and 175 mm long as depicted in Figure 2a. The sample has a saw cut inclined at 30 degrees to the vertical (z) axis to simulate a fault. The saw-cut surfaces were surface ground and then hand lapped with 600 grit abrasive (approximately 15 μm particle size) to produce a smooth uniform fault surface. The sample was mounted between steel end pieces and placed in a 4.8 mm-wall-thickness polyurethane sleeve to isolate it from the silicone oil that is used as a confining fluid. This configuration is shown in Figure 2b.

The sample assembly was placed in the pressure vessel and constant confining pressure p_c of 40, 80 or 120 MPa was applied during the test sequence. Axial stress σ_1 was then applied with a hydraulic ram that advanced a steel piston against the bottom of the sample column (Figure 2a). Axial displacement, x_{LP} , and axial stress, σ_1 , were measured outside the pressure vessel at the position identified as ‘load point’ in Figure 2a. Fault slip δ is not measured directly, but can be approximated by subtracting the elastic shortening of the sample column from the total axial displacement. Axial stress was applied by imposing a constant axial shortening rate $v_{LP} = d(x_{LP})/dt$. This type of loading causes the axial stress on the sample to slowly increase until a stick-slip instability spontaneously occurs. Stick-slip instabilities are associated with measureable fault slip, a sudden drop in the stress supported by the sample, and the intense radiation of seismic waves. The seismic waves are recorded by an array of 16 piezoelectric AE sensors that are glued onto the granite sample. Each sensor has a cylindrical piezoceramic element (PZT lead-zirconate-titanate) 6.35 mm in diameter and 2.54 mm thick. In the seconds just prior to each stick-slip instability, we recorded tens to hundreds of discrete AEs that are reminiscent of foreshocks. The AEs are not typically associated with externally measureable fault slip or

drops in stress. We located these AEs using standard inversion of arrival times and found that they are all located on the fault plane (to within our ± 2 mm precision).

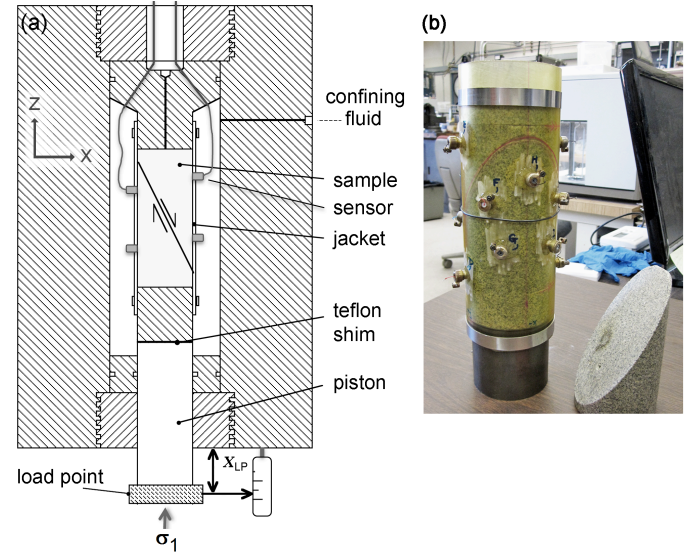


Fig. 2. Diagram (a) of sample mounted inside of pressure vessel and photo (b) of the test sample during assembly. Piezoelectric transducers are mounted in the brass fixtures attached to the sample. Adapted from McLaskey and Lockner, 2014.

In this work, no high-pass filters or preamps were employed in order to ensure wide-band recordings of signals from both the AEs and from stick-slip instabilities. While this limited the detection of small AEs, all of the largest AEs were detected and recorded [16]. The stick-slip events, on the other hand, were so energetic that signals passed directly to the digitizer were off scale after only a few microseconds. In order to capture the full transducer response from the stick-slip events, inputs were split and attenuated signals were recorded simultaneously.

3. ANALYSIS OF AE SPECTRA

3.1 Properties of an AE source and recorded waveforms

The source of an AE can be represented mathematically as a time-varying moment tensor $m_{ij}(t)$. The moment tensor is a collection of force couples that act in orthogonal directions and orientations. Each force couple may have a nonzero moment, but produces no net linear force in any one direction. As described above, the averaging of many different sensor's response makes it impossible to distinguish the directionality of the source therefore the tensor $m_{ij}(t)$ is reduced to the scalar $m(t)$. Similar to the way earthquakes are analyzed, we choose to use a frequency domain representation of the AE sources, and employ a Fourier transform to convert

recorded signals from the time domain to the frequency domain. In the frequency domain, the AE source can be represented by the AE source spectrum $M(f)$ which is the Fourier transform of $m(t)$. Similar to earthquakes, the seismic moment of the AE is equal to Ω_0 , the amplitude of the AE source spectrum $M(f)$ at low frequencies (below the AE corner frequency), as shown schematically in Figure 3.

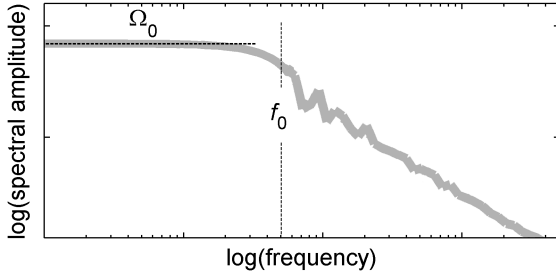


Fig. 3. Schematic example of the amplitude of the source spectrum of an AE, earthquake, or ball impact.

In typical AE analyses, only very short time recordings are used because the first few waves to be felt by the sensor are direct arrivals and are the simplest to model and easiest to interpret. Typical AE source location techniques use only the timing of the initial P wave arrival. AE moment tensor inversion schemes typically use only the first motion or amplitude of the initial P wave arrival and therefore solve for only the focal mechanism of the initiation of the event with no regard for time history $m(t)$. Examples of the first 20-30 microseconds of the signals recorded from six different sensors are shown in Figure 4a-f. The later part of the signal is typically termed the “coda” and it is the result of myriad reflections from the sides of the sample and a mechanical interaction with the loading frame or apparatus that houses the sample under test.

When estimating frequency content using a Fourier transform, the low frequency components of the signal are not well resolved when a short time window is employed. For example, it is impossible to accurately estimate the amplitude of the AE source spectrum at 10 kHz when only a 100 microsecond time window is employed for the calculation of the Fourier transform. In this work, we compare spectral estimates obtained from Fourier transforms that employ a variety of different time windows. Based on our experience using this multiple-window approach, we do not consider a spectral estimate to be reliable unless it is derived from a Fourier transform with a window length that is twenty times longer than the period of the lowest frequency considered. For example, to estimate an AE source spectrum down to 10 kHz, we employ time windows of at least 2 ms.

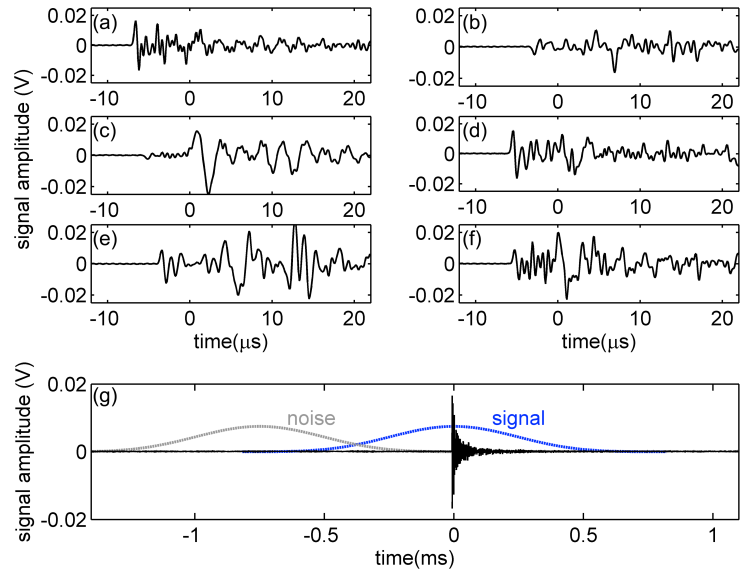


Fig. 4. Example signals from an example AE event recorded from the experiment described in Figure 2. (a-f), the first few microseconds of the recorded signals from six different sensors. The timing of initial wave arrivals is typically used to locate the AEs and determine focal mechanism. Fourier transforms derived from long time windows (g) are used to estimate the source spectra of the AEs. The data shown in (a) is a subset of that shown in (g).

Amplitude spectra are obtained from the Fourier transform of long sections of signals (i.e. 1-5 ms) centered on the first wave arrival and tapered with a Blackman-Harris window [17] as shown in Figure 4g. Figure 5a shows example spectra of three AEs alongside noise spectra. Noise spectra are derived using a window of identical length and taper but from a section of the recorded waveform before the first wave arrival (Figure 4g). Fourier spectra are resampled into equal intervals in log frequency at $\Delta \log_{10}(f) = 0.05$. Each resampled spectral estimate is shown as a symbol in Figures 5 and Figure 7 and is the average of spectral estimates from at least two Fourier frequencies.

For a single AE event, we observe some differences in spectra obtained from individual recordings from different sensors. Spectral differences are presumably due to differences in wave propagation effects such as increased attenuation for longer path lengths, geometrical spreading, radiation pattern of the source, and variation in sensor sensitivity with incidence angle. To reduce this variability, we average the spectra calculated from recordings from many different sensors. As described previously, this averaging eliminates our ability to discern the phase information or the directionality of the source, but it results in a more stable estimate of spectral amplitudes. Figure 5 shows spectral amplitudes derived from averages of 10-16 sensors' recordings.

3.2 Comparison of spectra of collocated AEs

In a standard empirical Green's function analysis, a small seismic event is used as a reference source for the study of a larger seismic event. The two seismic events must have nearly the same source location and must be recorded by the same sensors, because it is assumed that differences between the spectra of the two events are due to differences in the source $M(f)$, rather than differences in wave propagation or sensor response. This technique is frequently used to study earthquakes, and has also been for the study of AEs [18-20].

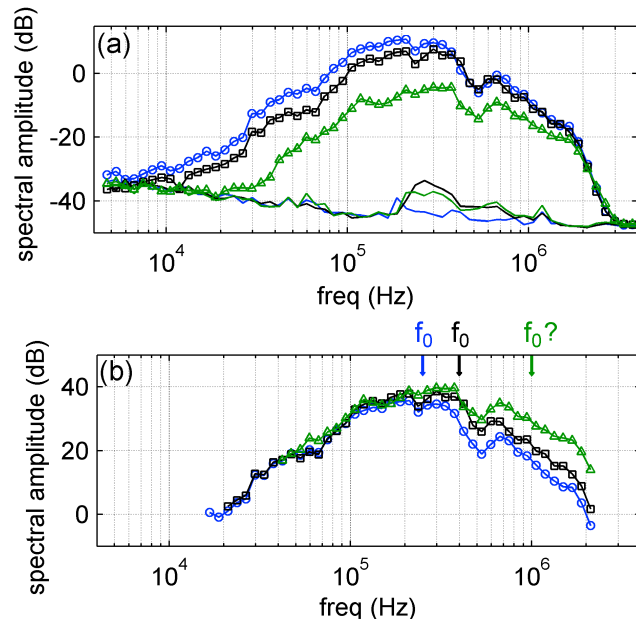


Fig. 5. (a) Amplitude of spectra from three collocated AEs compared to noise spectra (lines without symbols near the bottom of the plot). The three different colors correspond to spectra from three different collocated AEs. (b) Spectra are shown only in the frequency band with adequate signal-to-noise ratio and spectra are offset so that they agree at low frequencies. Adapted from McLaskey and Lockner, 2014.

Figure 5 shows the spectra of three AEs located within 5 mm of each other on the fault plane. Since an average raypath is about 60 mm, we will consider these events to be essentially co-located. In Figure 5b, the same three spectra are offset vertically 25, 31, and 44 dB so that they agree at low frequencies. The spectra of smaller AEs contain more high frequency energy relative to low frequency energy when compared to spectra of larger AEs. This is consistent with typical earthquake scaling behavior in which smaller seismic events typically have higher corner frequencies f_0 [21]. The spectral amplitude of the larger AE (blue curve with circles) starts to drop below that of the smaller AEs at about 200-300 kHz, which indicates that the corner frequency of the larger AE is roughly 200-300 kHz. The vertical offset required to make the amplitude of the AE source spectra match at frequencies below the corner frequency provides a

measure of the relative sizes (or seismic moments) of the AEs, but the absolute sizes remain unknown.

4. ABSOLUTE MEASURE OF AE SOURCE SPECTRA BASED ON BALL IMPACT

4.1 In-situ ball drop procedure

Absolute seismic moment is determined using a ball impact as a reference source or empirical Green's function. The absolute amplitude of the ball impact source spectrum at low frequencies (below the corner frequency) is equal to the ball's change in momentum during the collision, which can be easily calculated or estimated from the mass and velocity of the ball.

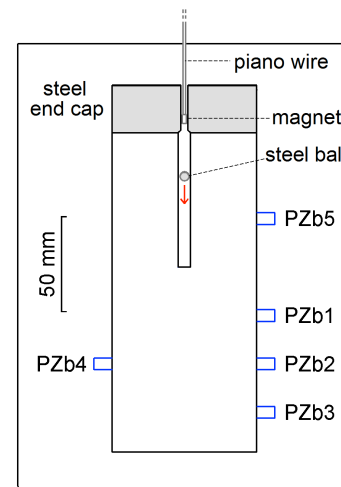


Fig. 6. Schematic diagram of the calibration sample which is identical to the test sample except instead of a saw cut fault it contains a cavity where a ball drop is performed with the aid of a magnet and piano wire. Adapted from McLaskey et al., 2015.

To use a ball impact as a reference source for the study of AEs, we must record signals from a ball impact source that occurs under conditions that are nearly identical to those of the AEs. For some experimental arrangements a ball can simply be dropped onto a free surface of the sample. However, for the triaxial loading configuration shown in Figure 2a, we assembled a special calibration sample, shown schematically in Figure 6. The calibration sample is identical to the test sample (Figure 2b), except that instead of a simulated fault, it contains a cavity in which ball impact can take place. A 4.76 mm diameter steel ball is placed in the cavity and a 3.2 mm diameter magnet is glued to the end of a 300 mm long section of piano wire. The piano wire extends out of the hole and out of the pressure vessel through a section of steel tubing. By manually pushing on the piano wire, the magnet can be lowered to the bottom of the hole. The steel ball adheres to the magnet and, by pulling on the wire, it can be lifted to the top of the hole. At this point, the ball is stopped by a hollow

cylindrical aluminum insert that is glued into a hole in the steel end cap. The hole in the insert is large enough to allow the wire and magnet to pass through but small enough to stop the ball. When the magnet is pulled away from the ball and into the insert, the ball falls 66.5 mm onto the flat surface at the bottom of the cavity. Seismic waves radiated from the point of impact propagate through the sample and are recorded by piezoelectric sensors (PZb1 – PZb5) glued directly on the granite calibration sample.

4.2 Estimating moment from low-frequency response

We compare signals from the ball impact described above to those from AEs located near the center of the test sample. We also choose combinations of sensors whose source-to-sensor ray path lengths and incidence angles are similar between the ball drop and the AE. We are careful to use identical windowing techniques on both the ball impact and AE data.

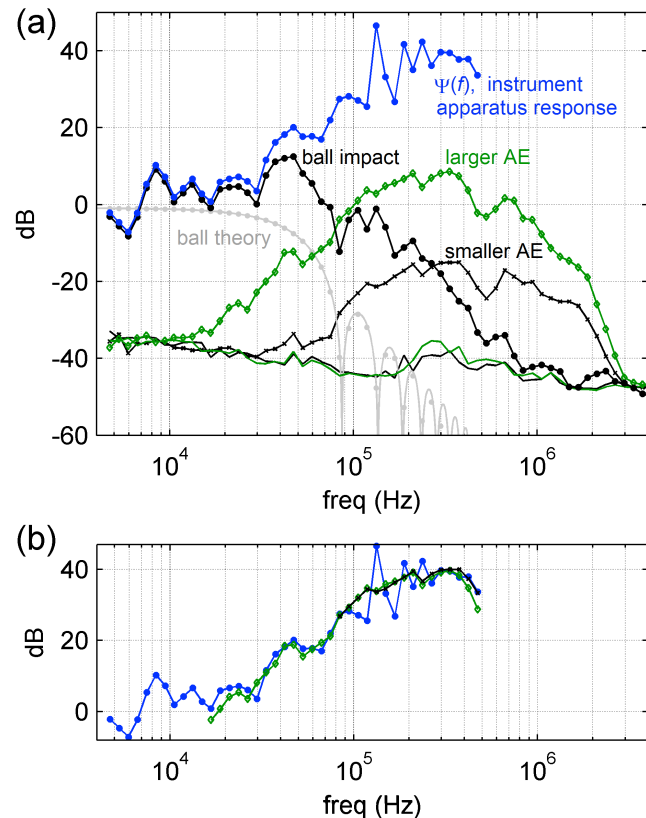


Fig. 7. (a) Amplitude of spectra of AEs (green diamonds and black tick marks) are compared to the amplitude of the spectrum of a ball impact (black circles). The instrument apparatus response (blue circles) is found by dividing the amplitude spectrum of the ball impact by the theoretical source spectrum of the ball (gray circles) (b) The spectra of the two AEs are compared to the instrument apparatus response spectrum derived from the ball impact data. Spectra are shown only in the frequency band with adequate signal-to-noise ratio and spectra are offset vertically so that they agree at low frequencies. Adapted from McLaskey et al., 2015.

Figure 7 shows the amplitude of spectra obtained from two different AE events located close to the center of the sample. The spectra shown are the average of spectra derived from 11 different sensors' recordings. The 11 sensors have an average source-to-sensor path length of 58 mm and average incidence angle of 49 degrees. Figure 7 also shows the amplitude of the spectrum of a ball impact performed inside the calibration sample at 40 MPa confining pressure. To obtain more stable spectral estimates above the ball's corner frequency, we calculate spectra from the average of spectra from five different ball drops. In addition to averaging over five ball drops, the ball impact spectrum shown in Figure 7 is the weighted average of spectra estimated from recordings at three stations (PZb1, PZb2, and PZb3, see Figure 2c). The weighted average ray path length (59 mm) and incidence angle (50 degrees) are nearly identical to those from signals used to calculate the spectra of the AEs.

Figure 7 also includes the spectrum of the impact source that we calculated theoretically using Hertz theory of impact for the characteristics of the current ball drop (4.76 mm diameter steel ball dropped 66 mm onto granite). The spectrum shown has been normalized by its long period level $\Omega_0 = m(v_0 + v_f) = 1 \times 10^{-3}$ Ns. In the above equation, m is the mass of the 4.76 mm diameter ball (0.432 g), v_0 is the incoming velocity of the ball and v_f is the rebound velocity of the ball. We calculate $v_0 = 1.2$ m/s from the 66.5 mm drop height, and we estimate $v_f = 1.0$ m/s from the 209 ms of travel time in air between the first and second bounces of the ball, which we can determine based on a long-time-window recording of seismic waves generated from two successive bounces. (Time windows used to obtain spectra include only one bounce.) The long period level Ω_0 of the ball impact source spectrum has units of momentum (force*time) rather than moment (force*distance). These two quantities can be related by a simple scale factor C_{FM} which was found to be equal to twice the speed of sound in the material from which the seismic sources arise [15] ($C_{FM} \approx 10$ km/s for the granite under pressure). Thus, the ball impact described above produces an equivalent seismic moment of 1×10^{-3} Ns $\times 10$ km/s = 10 Nm. We use the relation $M = 2/3 * \log_{10}(M_0) - 6.067$ [22] to find the moment magnitude $M = -5.4$.

We estimate the absolute seismic moment of the AEs by comparing the AE spectral amplitude below the corner frequency with the spectral amplitude of the ball impact below its corner frequency. The corner frequency of this ball impact is around 30 kHz which is near the lower bound of the usable frequency band where the AE recordings have good signal-to-noise ratio. To compensate for the spectral falloff above the corner frequency, the ball impact spectrum is divided by the

theoretical spectrum. The result is termed the instrument apparatus response spectrum ($\Psi(f)$). In principle, $\Psi(f)$ approximates the average transfer function for the entire test system, that is, the response that should be observed for a white noise source. This spectrum is also plotted in Figure 7.

Just as relative seismic moment can be determined by the vertical offset required for spectra to overlay each other at frequencies below the corner frequency, absolute moment can be determined by the vertical offset required for AE spectra to overlay the ball drop spectrum at low frequencies. Figure 7b shows the two AE spectra and $\Psi(f)$ derived from the ball impact spectrum shown in Figure 7a but the AE spectra are offset vertically 31 and 54 dB to match $\Psi(f)$ at low frequencies. Since these spectra are a good match to the apparatus response spectrum to at least 200 kHz, their corner frequencies are probably above this. We would expect that larger AEs with lower corner frequencies would have spectra that drop below $\Psi(f)$ at high frequencies. Based on the vertical shift of the spectra, the larger AE is 31 dB smaller than the ball impact ($M_0 = 0.3$ Nm, $\mathbf{M} = -6.4$) and the smaller AE is 54 dB smaller than the ball impact ($M_0 = 0.02$ Nm, $\mathbf{M} = -7.2$).

Due to averaging, the ball drop and AE do not need to be precisely collocated. When the output of many sensors is averaged, the spectral estimates are largely insensitive to variation in AE source location within the sample. This allows us to estimate the seismic moment of all of the AEs recorded on the sample, not just the ones that are collocated with the ball drop. The insensitivity to AE location is also important since, in the majority of cases, ball impact occurs on the surface of the sample while AEs occur within the interior. McLaskey et al. [15] demonstrated how, with a little care to avoid Rayleigh waves and other potential complications, the empirical system calibration could be used for ball impact and AEs that are not at all collocated, provided that the sample is homogeneous.

Figure 8 shows the distribution of AE sizes for about 400 AEs recorded during a sequence of stick-slip instabilities. The vertical dashed line indicates the approximate level of completeness determined from triggering criteria [16]. The smallest events shown are around $\mathbf{M} = -8$, but these are recorded without amplification prior to digitization. In other AE studies, gains of 40 to 60 dB are common, and very small events are recorded that would not register with the present experimental setup. Thus we anticipate that $\mathbf{M} = -9$ or smaller AEs are routinely recorded in other AE tests.

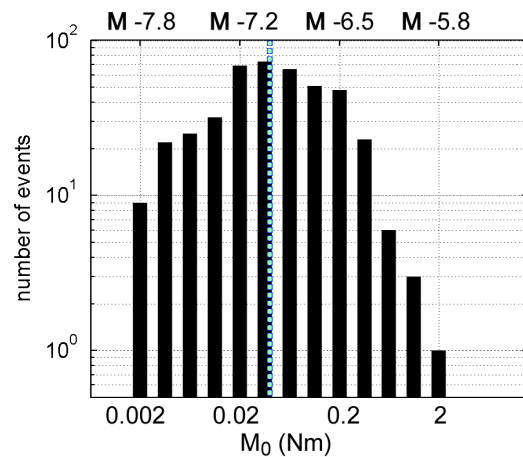


Fig. 8. Distribution of the sizes of about 400 AEs recorded in a series of stick-slip instabilities. The vertical dashed line indicates the approximate level of completeness determined from triggering criteria [16].

Using the same calibration technique, we studied the source spectra of the stick-slip events that rupture the entire simulated fault in the saw cut granite sample when under 80 MPa of confining pressure. We estimate that the corner frequency for these larger events is about 20-30 kHz, and based on the amplitude of the source spectra at low frequencies we estimated that their seismic moment is about 1×10^4 Nm ($\mathbf{M} = -3.5$).

5. DISCUSSION

It has long been thought that the small size of AEs relative to grain size of rock causes their physics to diverge from that of larger earthquakes [1]. For example, AEs produced from intact rock samples without a pre-existing fault are thought to be the result of microcrack growth due to grain scale stress heterogeneity [1], and as a result they often have tensile or complex source focal mechanisms. Because of the preexisting smooth fault in the current experiments, ambient stresses are significantly below the levels needed for damage to occur within the intact rock mass (typically 20 to 40 percent lower). The AE events we have analyzed occur on the preexisting fault surface and have simple double-couple mechanisms [16].

The largest AEs recorded have seismic moments $M_0 = 0.3 - 3$ Nm ($\mathbf{M} = -6.4$ to -5.7). Based on spectral estimates, such as those shown in Figure 5, we can roughly estimate corner frequency f_0 of these AEs to be 200-300 kHz. We assume the Brune [23] relationship between f_0 and source dimension $r_0 = 2.34 \beta / (2\pi f_0)$ and calculate stress drop $\Delta\sigma = 7/16 M_0 r_0^{-3}$. These calculations imply source dimensions of 4-6 mm and stress drops of 0.6-7.5 MPa. (We assume $\beta = 3200$ m/s, since most of the wave energy arrives with the S wave.)

Figure 9 compares the characteristics of the AEs and stick-slip instabilities reported here to other laboratory generated seismic events, mining induced earthquakes, and natural earthquakes of all sizes. The source dimensions and magnitudes of the AEs are much smaller than those of larger natural earthquakes, but the stress drops are similar which suggests that the same source scaling relationship applies to earthquakes and AEs. On the other hand, the larger stick-slip instabilities appear to have stress drops that are somewhat higher. This difference may be related to the fact that the AEs, like common earthquakes, are fully contained within the fault plane, and therefore ‘feel’ the stiffness of the surrounding rock, while stick-slip instabilities rupture the entire fault surface and are driven by interaction with the more compliant loading frame [24]. Further work is required to establish how the mechanics of stick-slip instabilities scale and whether or not they are truly different from earthquakes.

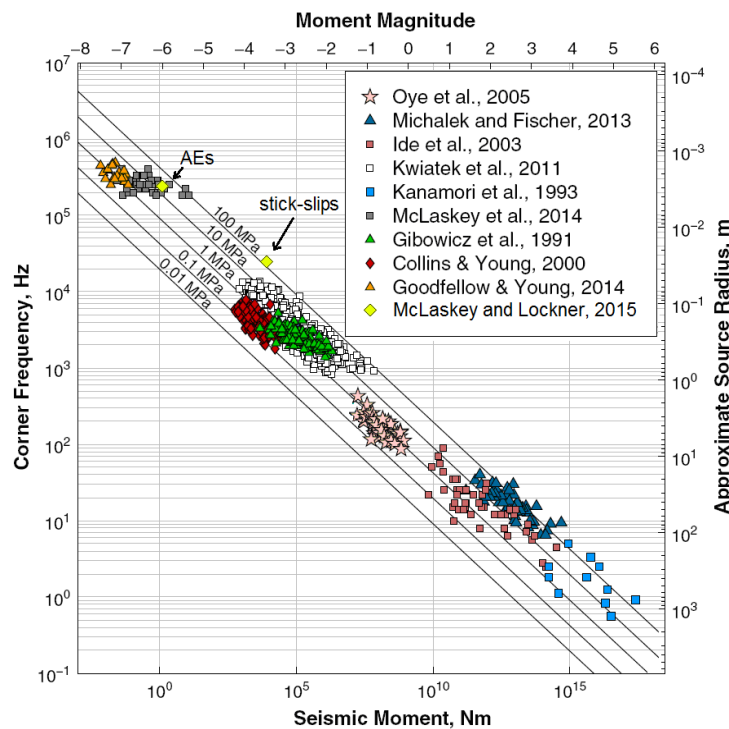


Fig. 9. AE and stick-slip source parameters are compared to other laboratory generated seismic events, mining induced earthquakes, and natural earthquakes. Adapted from Goodfellow and Young [31].

Over the course of an individual loading cycle (culminating in a stick-slip event), the imposed constant loading rate causes average stress on the sawcut fault to continuously rise. During this process, an individual AE event causes redistribution of local stress, essentially shedding stress concentrated at one location to the adjacent fault surface. As the average stress increases, neighboring regions become less able to accommodate this stress rise without also failing. In this way, individual AEs probe the stress state of the adjacent fault

until eventually one event (not necessarily the largest AE event in the sequence) cascades into a global stick-slip event. McLaskey and Lockner [16] showed that the recorded waveforms from the initiation of stick-slip events are essentially indistinguishable from waveforms of the largest AEs. Indeed, the onset of stick-slip can be precisely located from first arrivals just as AE sources are located [3, 16]. This suggests that stick-slip events are the result of AEs that grew considerably larger and ruptured the entire fault surface.

The frequency-magnitude distribution plotted in Figure 8 shows a distinct gap between the moments of the largest recorded AEs (3 Nm) and moments of the stick-slip events ($\sim 10^4$ Nm). The largest AEs have apparent source dimensions of 4-6 mm which is about an order of magnitude larger than the grain size in the Westerly granite and an order of magnitude smaller than the 76 x 152 mm fault surface. It is certainly possible that the dimensions of the AEs (4-6 mm) have been overestimated by the Brune model, but since AEs on the saw-cut surface appear to have the ability to grow larger (described above), we believe that they are probably less affected by grain size than the fault surface roughness. In this experiment, fault surfaces were ground flat and therefore have limited long wavelength topography. As a result, AEs that become larger than a specific size (in this case a few mm) are unlikely to be stopped by heterogeneity of fault stress or strength and will rupture the entire fault to produce a stick-slip instability. The calibration techniques described in this paper make it possible for this hypothesis to be tested against experiments on a rougher sample or a surface whose roughness distribution is not truncated by surface grinding.

ANOWLEDGEMENTS

The authors would like to thank Ole Kaven, Brian Kilgore, and two anonymous reviewers for helpful reviews of the manuscript.

REFERENCES

1. Lockner, D. A. 1993. Role of acoustic emission in the study of rock fracture, *Int. J. Rock Mech. Min. Soc. Geomech. Abstr.*, 30, 884–899.
2. Lei, X., Kusunose, K., Satoh, T., and Nishizawa, O. 2003. The hierarchical rupture process of a fault: an experimental study, *Phys. Earth. Planet. Inter.* 137, 213–228.
3. Thompson, B. D., Young, R. P. and Lockner, D. A. . 2009. Premonitory acoustic emissions and stick-slip in natural and smooth-faulted Westerly granite, *J. Geophys. Res.*, 114, B02205.
4. Johnson, P., B. Ferdowsi, B. Kaproth, M. Scuderi, M. Griffa, J. Carmeliet, R. Guyer, P. Y. Le Bas, D. Trugman, and C. Marone . 2013. Acoustic emission and microslip

- precursors to stick - slip failure in sheared granular material, *Geophys. Res. Lett.*, 40(21), 5627-5631. doi:10.1002/2013GL057848
5. Goebel, T. H. W., T. Candela, C. G. Sammis, T. W. Becker, G. Dresen and D. Schorlemmer . 2014. Seismic event distributions and off-fault damage during frictional sliding of saw-cut surfaces with pre-defined roughness *Geophys. J. Int.* 196 (1): 612-625. doi: 10.1093/gji/ggt401
 6. Hsu, N., and F. Breckenridge . 1981. Characterization and calibration of acoustic emission sensors, *Materials Eval.* 39, 60-68.
 7. Oppenheim, A., A. Willsky, and I. Young. 1983. *Signals and Systems* (Prentice-Hall) USA
 8. McLaskey, G. C. and S. D. Glaser . 2012. Acoustic Emission Sensor Calibration for Absolute Source Measurements, *J. Nondestruct. Eval.* 31, 157-168.
 9. McLaskey, G. C., B. D. Kilgore, D. A. Lockner, and N. M. Beeler. 2014. Laboratory generated M -6 Earthquakes, *Pure Appl. Geophys.* 31, 157-168. doi: 10.1007/s00024-013-0772-9.
 10. Frankel, A., and H. Kanamori. 1983. Determination of rupture duration and stress drop from earthquakes in southern California, *Bull. Seismol. Soc. Am.*, 73, 1527-1551
 11. Mueller, C., S. 1985. Source pulse enhancement by deconvolution of an empirical Green's function, *Geophys. Res. Lett.* 12, 33-36 doi:10.1029/GL012i001p00033
 12. Hutchings, W., and F. Wu . 1990. Empirical Green's functions from small earthquakes: A waveform study of locally recorded aftershocks of the 1971 San Fernando earthquake, *J. Geophys. Res.* 95, 1187-1214.
 13. Hough, S. E., and D. S. Dreger. 1995. Source parameters of the 23 April 1992 M 6.1 Joshua Tree, California, earthquake and its aftershocks: Empirical Green's function analysis of GEOS and TERRA scope data, *Bull. Seismol. Soc. Am.*, 85, 1576-1590, 1995.
 14. Goldsmith, W. 2001. *Impact* (Dover Publications), New York.
 15. McLaskey, G. C., D. A. Lockner, B. D. Kilgore, and N. M. Beeler. 2015. A Robust Calibration Technique for Acoustic Emission Systems Based on Momentum Transfer from a Ball Drop, *Bull. Seismol. Soc. Am.*, 105(1), 257-271 doi: 10.1785/0120140170
 16. McLaskey, G. C., and D. A. Lockner . 2014. Preslip and cascade processes initiating laboratory stick-slip, *J. Geophys. Res. Solid Earth*, 119, doi:10.1002/2014JB011220.
 17. Harris, F. 1978 On the use of windows for harmonic analysis with discrete Fourier transform, *Proc. IEEE* 66, (1), 51-83
 18. Dahm, T. 1996. Relative moment tensor inversion based on ray-theory: theory and synthetic tests, *Geophys. J. Int.* 124, 245-257.
 19. Sellers, E. J., M. O. Kataka, and L. M. Linzer. 2003. Source parameters of acoustic emission events and scaling with mining-induced seismicity, *J. Geophys. Res.* 108, B9 2418.
 20. Kwiatek, G., K. Plenkers, and G. Dresen . 2011. Source parameters of picoseismicity recorded at Mponeng Deep Gold Mine, South Africa: Implications for scaling relations, *Bull. Seismol. Soc. Am.*, 101(6), 2592-2608, doi:10.1785/0120110094.
 21. Aki, K. 1967. Scaling law of seismic spectrum, *J. Geophys. Res.*, 72, 1217-1231.
 22. Hanks, T. C., and H. Kanamori . 1979. A moment magnitude scale, *J. Geophys. Res.*, 84, 2348-2350.
 23. Brune, J. N. 1970. Tectonic stress and spectra of seismic shear waves from earthquakes, *J. Geophys. Res.* 75, 4497-5009.
 24. McGarr. A. 2012. Relating stick-slip friction experiments to earthquake source parameters, *Geophys. Res. Lett.*, 39, L05303.
 25. Oye, V., H. Bungum, and M. Roth . 2005. Source parameters and scaling relations for mining-related seismicity within the Pyhäsalmi ore mine, *Bull. Seismol. Soc. Am.*, 95, 1011-1026.
 26. Michalek, J., and T. Fischer . 2013. Source parameters of the swarm earthquakes in West Bohemia/Vogtland, *Geophys. J. Int.*, 195, 1196-1210.
 27. Ide, S., G. Beroza, S. Prejean, and W. Ellsworth . 2003. Apparent break in earthquake scaling because of path and site effects on deep borehole recordings, *J. Geophys. Res.*, 108(B5), 2271, doi:10.1029/2001JB001617.
 28. Kanamori, H., J. Mori, E. Hauksson, T. H. Heaton, L. K. Hutton, and L. M. Jones . 1993. Determination of earthquake energy release and ML using TERRAScope, *Bull. Seismol. Soc. Am.*, 83, 330-346.
 29. Gibowicz, S. J., R. P. Young, S. Talebi, and D. J. Rawlence . 1991. Source parameters of seismic events at the Underground Research Laboratory in Manitoba, Canada: Scaling relations for events with moment magnitude smaller than 2, *Bull. Seismol. Soc. Am.*, 81, 1157-1182.
 30. Collins, D. S., and R. P. Young . 2000. Lithological Controls on Seismicity in Granitic Rocks, *Bull. Seismol. Soc. Am.*, 90, 709-723.
 31. Goodfellow, S.D. and R. P. Young . 2014. A laboratory acoustic emission experiment under in situ conditions, *Geophys. Res. Lett.* 41, doi:10.1002/2014GL059965.